Aerodynamic integration produces a vehicle shape with a negative drag coefficient

Kambiz Salari[a] and Jason M. Ortega[a,1]

[a]Lawrence Livermore National Laboratory, Livermore, CA 94551

Edited by John A. Rogers, Northwestern University, Evanston, IL, and approved June 10, 2021 (received for review April 13, 2021)

Negative drag coefficients are normally associated with a vessel outfitted with a sail to extract energy from the wind and propel the vehicle forward. Therefore, the notion of a heavy vehicle, that is, a semi truck, that generates negative aerodynamic drag without a sail or any external appendages may seem implausible, especially given the fact that these vehicles have some of the largest drag coefficients on the road today. However, using both wind tunnel measurements and computational fluid dynamics simulations, we demonstrate aerodynamically integrated vehicle shapes that generate negative body-axis drag in a crosswind as a result of large negative frontal pressures that effectively "pull" the vehicle forward against the wind, much like a sailboat. While negative body-axis drag exists only for wind yaw angles above a certain analytical threshold, the negative frontal pressures exist at smaller yaw angles and subsequently produce body-axis drag coefficients that are significantly less than those of modern heavy vehicles. The application of this aerodynamic phenomenon to the heavy vehicle industry would produce sizable reductions in petroleum use throughout the United States.

aerodynamics | drag | computational fluid dynamics | wind tunnel

Future reductions in petroleum use and carbon emissions will rely heavily upon improved heavy vehicle freight efficiency. Within the United States, domestic freight is dominated by heavy vehicles, that is, semi trucks, which handle approximately 81% of the total freight weight and nearly 86% of the total value of freight shipments (1). Although heavy vehicles comprise just 4% of all on-road vehicles, they are responsible for more than 20% of all transportation-related fuel consumption and greenhouse gas emissions (1). One of the main sources of inefficiency contributing to the low fuel economy [~6 mpg or 2.6 km/L (2)] of heavy vehicles is their relatively large body-axis drag coefficient $C_{Db} = D_b/(1/2)\rho V^2 A$ [C_{Db} can range upward of 0.8 to 1.8 (3–6), compared to 0.3 for a sedan (7) and 0.4 for an SUV (8)], where the body-axis drag force, D_b, is given by

$$D_b = D_w \cos\psi - S_w \sin\psi, \qquad [1]$$

where ρ is the density of air, V is the characteristic wind speed, A is the frontal projection area of the vehicle, D_w is the wind-axis drag force, S_w is the wind-axis side force, and ψ is the yaw angle of the vehicle relative to the oncoming wind (Fig. 1*A*). At highway speed (104.6 km/h or 65 mph), the Reynolds number, $\mathrm{Re} = \rho V w/\mu$, for a heavy vehicle is about 5×10^6, and, as such, the drag force is mostly due to pressure, not viscous shear, on the vehicle surface, where w is the vehicle width, and μ is the dynamic viscosity of air. Poor aerodynamics promote parasitic losses not only for the vehicle traveling directly into the wind ($\psi = 0°$), as would be the case for quiescent weather, but also for the more common scenario of traveling in a crosswind. At the vehicle midheight (2.1 m), the average crosswind throughout North America is about 11.3 km/h (7 mph) (3), translating to $1.4° \le |\psi| \le 6.1°$ at highway speed and assuming that the crosswind approaches the vehicle with equal probability from any direction (9, 10). Recent efforts have focused upon reducing the aerodynamic drag of heavy vehicles by installing multiple drag reduction devices (11, 12). For example, boat-tail (BT) plates (13, 14) increase the trailer base pressure in quiescent and crosswind conditions, while trailer skirts (15) and tractor side and roof extenders (16), both of which have become widely utilized in recent years (17), function by decreasing the amount of crosswind flow impinging upon the front faces of the trailer and the trailer wheels, respectively (Fig. 1*B*). While these simple devices produce notable reductions in C_{Db} (Fig. 1*C*), more substantial gains are inherently limited by the rather fixed shape of modern heavy vehicles. A radical solution to this restriction is to completely reshape the exterior of the heavy vehicle, so that it is aerodynamically integrated along its entire length l in a smooth, continuous fashion and not through an ad hoc patchwork of separate add-on devices (Fig. 1*B*). Following this approach here, an investigation was conducted on highly streamlined vehicle shapes that not only have significant reductions in aerodynamic drag but also exhibit negative values of C_{Db} beyond a threshold yaw angle.

To evaluate the performance of such vehicle shapes, the aerodynamic forces on two 1/8th-scale generic speedforms (GSF1 and GSF2; Fig. 1*D*) were measured in a closed-circuit wind tunnel (see *Materials and Methods*). Although both shapes largely follow the overall proportions of a modern heavy vehicle, the cargo trailer is reshaped, and the underbody, wheels, tractor-trailer gap, and all exterior details were completely removed to yield an upper bound on the efficiency gains. GSF2 is slightly more streamlined than GSF1 by incorporating larger frontal corner radii (3), shallower hood and windshield angles, greater trailer tear-dropping, and a longer BT. Over the entire range of yaw angles commonly seen in operation, this exterior reshaping produces substantial reductions in C_{Db} compared to that of modern heavy vehicle outfitted with add-on devices (Fig. 1*C*). With increasing yaw angles, this benefit continues to increase, as evidenced by the decreasing values of C_{Db}. This indicates that the geometry is passively extracting energy from the freestream to counteract the body-axis drag force, which would have otherwise increased with ψ. When $|\psi| > 18°$ [an angle that can likely be encountered in more-windy states, such as Wyoming, when operating at highway speed within a 32 km/h (20 mph) crosswind (18)], the body-axis drag force is completely counteracted, and C_{Db} becomes negative for GSF2. Subsequently, the vehicle "pulls" itself forward against the wind, much like a sailboat. This beneficial, counterintuitive behavior for a streamlined body was previously demonstrated on a truncated, very low aspect ratio ($w/l = 0.37$) airfoil planform for $|\psi| > 24°$ and attributed to the large negative pressures that arise on the front leeward side (19). However, when this concept was applied to the front end of a heavy vehicle with a conventional trailer, C_{Db} remained

K.S. and J.M.O. designed research, performed research, analyzed data, and wrote the paper.

The authors declare no competing interest.

[1]To whom correspondence may be addressed. Email: ortega17@llnl.gov.

Published June 28, 2021.

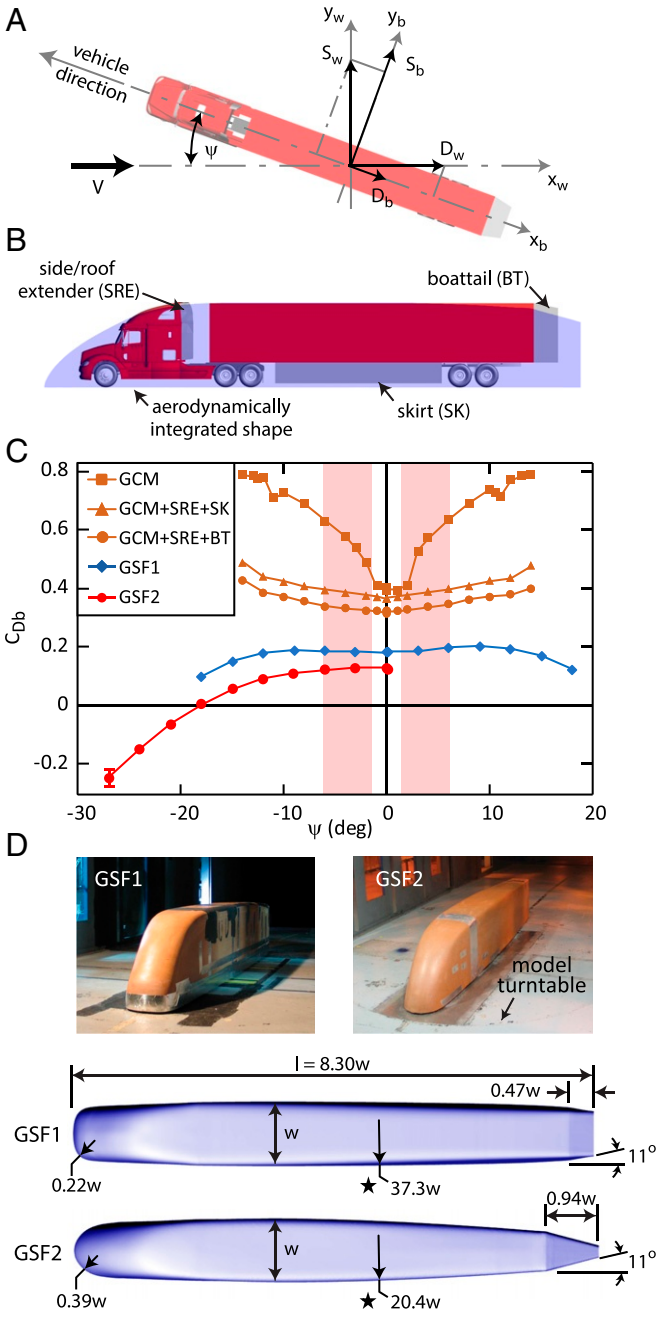

Fig. 1. (*A*) Aerodynamic forces acting upon a heavy vehicle yawed relative to the oncoming wind. (*B*) Drag reduction techniques using either ad hoc add-on devices or smooth aerodynamic integration and (*C*) the corresponding body-axis drag coefficient, C_{Db}, versus yaw angle, ψ, where the data for the 1/8th-scale generic conventional model (GCM) of a modern heavy vehicle is taken from ref. 6. The red shading from $1.4^\circ \leq |\psi| \leq 6.1^\circ$ is the range of wind yaw angles typically experienced for a vehicle traveling at highway speed (104.6 km/h or 65 mph) (9). (*D*) GSF shapes 1 and 2, where w = 0.324 m at 1/8th scale. The ★ denotes the tear-dropping radius of curvature.

greater than zero for all yaw angles measured up to 55°, although notable reductions in C_{Db} were observed. Similarly, Cooper (20) investigated a heavy vehicle that was streamlined in a coarse, piecewise manner, and, although C_{Db} decreased with increasing ψ, negative values of C_{Db} were not measured.

A simple criterion for determining when C_{Db} is less than zero can be obtained from Eq. **1** to yield $|C_{Dw}/C_{Sw}| < \tan|\psi|$. The ratio $|C_{Dw}/C_{Sw}|$ is essentially the inverse of the lift-to-drag ratio of an airfoil, to which the body is analogous when viewed from above (Fig. 1*A*). A plot of this criterion, along with measurements of $|C_{Dw}/C_{Sw}|$ (Fig. 2*A*), highlights the potential to extract even more energy from the freestream by further decreasing the values of $|C_{Dw}/C_{Sw}|$. While this can readily be accomplished through the installation of a sail (21) or vertical fins (22) as is the case for wind-assisted vehicles, a more practical approach for a heavy vehicle is through additional frontal streamlining. Computational fluid dynamics (CFD) simulations (see *Materials and Methods*) of the resulting GSF3 shape, which has a longer nose with larger corner radii (Fig. 2*B*) than that of GSF2, demonstrate a wider range of ψ in which C_{Db} is less than zero due to the large region of negative pressures produced on the front leeward side (Fig. 2*C*). The ad hoc shape modifications used to produce the GSF3 shape are by no means optimal from both aerodynamic and operational standpoints. Although the reductions in drag come from additional frontal streamlining, particular attention must be paid to the entire shape. For subsequent designs, aerodynamic shape optimization techniques should be employed to preserve the useful cargo volume within the aerodynamically integrated shape while minimizing the value of C_{Db} and addressing any possible effects upon the vehicle stability within crosswinds.

The future application of smooth aerodynamic integration can have a fundamental impact upon the heavy vehicle freight

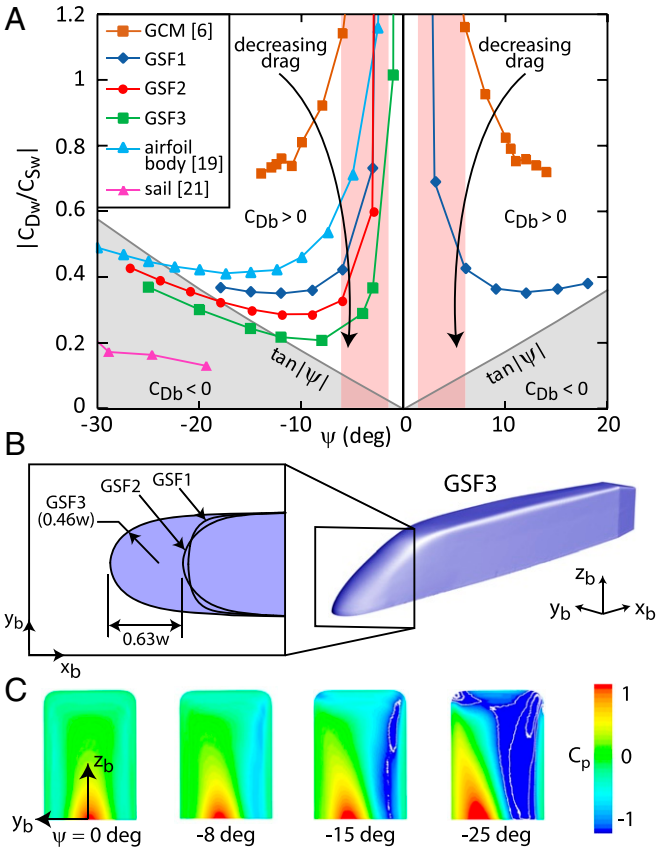

Fig. 2. (*A*) Ratio of the wind-axis drag and side force coefficients as a function of the yaw angle, ψ. The red shading from $1.4^\circ \leq |\psi| \leq 6.1^\circ$ is the typical range of wind yaw angles experienced for a vehicle traveling at highway speed (104.6 km/h or 65 mph) (9). The gray shading denotes the regime in which the body-axis drag coefficient, C_{Db}, is less than zero, that is, where $|C_{Dw}/C_{Sw}| < \tan|\psi|$. (*B*) Views of GSF3. (*C*) Pressure coefficient, $C_p = \Delta p/(1/2)\rho V^2$, on the front of the GSF3 computed from CFD simulations, where Δp is the pressure difference relative to atmospheric pressure. The white contour lines are for $C_p = -1$, -1.5, and -2.

sector, which consumed over 30 billion gallons of diesel fuel in 2017 (2). Given the estimate (17) that every 1% reduction in C_{Db} leads to a 0.45% reduction in fuel use for a heavy vehicle at highway speeds, the values of C_{Db} presented in this study highlight the potential to produce a significant reduction in both petroleum consumption and carbon emissions throughout the United States.

Materials and Methods

Wind Tunnel Investigation. The wind tunnel measurements are made in the NASA Ames 7 × 10 wind tunnel, which has a contraction ratio of 14:1, a test section size of 2.134 m × 3.048 m, and freestream turbulence intensity of 0.25%. The wind tunnel is operated at a nominal dynamic pressure of 3,100 Pa that is measured from a pressure ring upstream of the tunnel test section. Since the wind tunnel Re (1.63×10^6) is about 31% that of a heavy vehicle operating at highway conditions, measurements are made over a range of Re to ensure Reynolds number independence, which has also been shown for a similar heavy vehicle model investigated within this wind tunnel at the same scale and Reynolds number (23). The GSF models comprise an aluminum, steel, and wooden backbone to which is attached foam and a layer of modeling clay that can readily be reshaped during testing. Each GSF model is mounted on an external six-component balance at a height of approximately 0.02 m above the stationary wind tunnel floor. This height offset is equal to the nominal, tunnel floor boundary layer displacement thickness along the vehicle length, an approach that has been suggested to allow for correct, effective underbody clearance above a stationary ground plane (24, 25). The absence of a more realistic moving ground plane beneath the heavy vehicle models has been shown to have only a small effect (∼1%) on the resulting drag coefficient measurements (26). The models are yawed relative to the freestream by a turntable that can rotate to within $\pm 0.1^\circ$. The measurement uncertainty of the calculated force coefficients is ±0.03. For each data point collected during an experimental run, the force balance signals are sampled for 30 s (816 model lengths).

Computational Investigation. The flow field about GSF3 is found by solving the Reynolds-averaged Navier–Stokes equations (27) with a finite-volume CFD code (Star-CCM+, Siemens). The turbulent quantities are computed using the k$\omega-$SST (shear stress transport) turbulence model with an all-y^+ wall treatment model (28). The governing equations are solved on an unstructured, hexahedral cell mesh, which comprises a Cartesian core mesh and several layers of hexahedral prismatic cells extruded from the walls. Between these two meshes are transitional, polyhedral cells. The near-wall prism layer cell thickness is chosen such that the y^+ values are equal to 50, on average, over the surface of GSF3. The GSF3 geometry is obtained by three-dimensionally scanning the surface of GSF2 and streamlining the frontal region (longer frontal nose and larger corner radii; Fig. 2*B*) through the use of a CAD software package (Rhino 3D, Robert McNeel & Associates). The GSF3 model is scaled up to full size, that is, $w = 2.592$ m, and the simulations are conducted for ψ ranging from 0° to 25°. To better replicate real-world operating conditions, the inlet velocity to the computational domain ($380w \times 150w \times 620w$ in size) is chosen such that the freestream speed in the body-axis direction is 104.6 km/h (65 mph) for each ψ, and a moving ground velocity boundary condition is set to 104.6 km/h (65 mph) in the body-axis direction. A slip velocity boundary condition is prescribed to the walls of the computational domain, and the computed variables are extrapolated at the outlet to the computational domain. A no-slip velocity boundary condition is applied to the surface of GSF3. The nominal spatial resolution about GSF3 results in mesh sizes of approximately 200×10^6 cells. To demonstrate that the flow fields are adequately resolved by this level of resolution, the solution for GSF3 at $\psi = 4^\circ$, by way of example, is computed on four meshes with sizes of 6×10^6, 30×10^6, 172×10^6 (nominal), and 300×10^6 cells. Since the body-axis drag and side force coefficients exhibit a monotonic mesh convergence trend and grid convergence indexes of $GCI_{\text{nominal}} = 6 \times 10^{-3}$ and 2×10^{-4}, respectively, it was concluded that the nominal spatial resolution is adequate for the present study, where a conservative value of three is chosen for the safety factor F_s (29). The simulations are subsequently run on 400 cores (Intel Xeon E5-2670, 2.6 GHz).

Data Availability. All study data are included in the main text.

ACKNOWLEDGMENTS. We thank L. Slezak of the Department of Energy (DOE) Vehicle Technologies Program and D. Anderson of the DOE Energy Efficient Mobility Systems Program for their research support and funding; and C. Czlapinski and K. Timmerman of Navistar, Inc. and B. Porter, N. Gold, and the technical staff of NASA Ames Research Center for their assistance during the testing procedure. This work (LLNL-JRNL-821128) was performed under the auspices of the US DOE by Lawrence Livermore National Laboratory under Contract DE-AC52-07NA27344.

1. J. J. Brogan *et al.*, *Freight Transportation Modal Shares: Scenarios for a Low-Carbon Future* (Office of Energy Efficiency & Renewable Energy, 2013).
2. S. C. Davis, R. G. Boundy, *Transportation Energy Data Book: Edition 37.1* (Oak Ridge National Laboratory, 2019).
3. F. T. Buckley, W. H. Walston, C. H. Marks, Fuel savings from truck aerodynamic drag reducers and correlation with wind-tunnel data. *J. Energy* **2**, 321–329 (1978).
4. V. U. Muirhead, E. J. Saltzman, Reduction of aerodynamic drag and fuel consumption for tractor-trailer vehicles. *J. Energy* **3**, 279–284 (1979).
5. K. R. Cooper, The wind-tunnel simulation of surface vehicles. *J. Wind Eng. Ind. Aerod.* **17**, 167–198 (1984).
6. B. L. Storms, D. R. Satran, J. T. Heineck, S. M. Walker, "A study of Reynolds number effects and drag-reduction concepts on a generic tractor-trailer" in *34th AIAA Fluid Dynamics Conference and Exhibit* (American Institute of Aeronautics and Astronautics, 2004).
7. L. Tsuei, O. Savaş, Transient aerodynamics of vehicle platoons during in-line oscillations. *J. Wind Eng. Ind. Aerod.* **89**, 1085–1111 (2001).
8. J. Howell, C. Sherwin, M. Passmore, G. Le Good, Aerodynamic drag of a compact SUV as measured on-road and in the wind tunnel. *J. Passenger Car Mech. Syst. J.* **111**, 583–590 (2002).
9. SAE International, Wind tunnel test procedure for trucks and buses. http://www.sae.org/technical/standards/J1252_201207. Accessed 1 March 2021.
10. K. R. Cooper, "Truck aerodynamics reborn–lessons from the past" (Pap. 2003-01-3376, SAE International, 2003).
11. J. Ortega, K. Salari, A. Brown, R. Schoon, "Aerodynamic drag reduction of class 8 heavy vehicles: A full-scale wind tunnel study" (Rep. LLNL-TR-628153, Lawrence Livermore National Laboratory, 2013).
12. H. Choi, J. Lee, H. Park, Aerodynamics of heavy vehicles. *Annu. Rev. Fluid Mech.* **46**, 441–468 (2014).
13. J. D. Coon, K. D. Visser, "Drag reduction of a tractor-trailer using planar boat tail plates" in *The Aerodynamics of Heavy Vehicles: Trucks, Buses and Trains*, R. McCallen, F. Browand, J. Ross, Eds. (Springer, 2004), pp. 249–265.
14. F. Browand, C. Radovich, M. Boivin, "Fuel savings by means of flaps attached to the base of a trailer: Field test results" (Pap. 2005-01-1016, SAE International, 2005).
15. R. E. Schoon, "On-road evaluation of devices to reduce heavy truck aerodynamic drag" (Pap. 2007-01-4294, SAE International, 2007).
16. K. R. Cooper, "The wind tunnel testing of heavy trucks to reduce fuel consumption" (Pap. 821285, SAE International, 1982).
17. National Research Council, *Review of the 21st Century Truck Partnership: Second Report* (The National Academies Press, 2012).
18. B. E. Martner, J. D. Marwitz, Wind characteristics in southern Wyoming. *J. Appl. Meteorol.* **21**, 1815–1827 (1982).
19. R. N. Retzlaff, P. B. Hertz, "Airfoil plan-view body shapes to reduce drag at yaw" (Pap. 900314, SAE International, 1990).
20. K. R. Cooper, "Commercial vehicle aerodynamic drag reduction: Historical perspective as a guide" in *The Aerodynamics of Heavy Vehicles: Trucks, Buses and Trains,* R. McCallen, F. Browand, J. Ross, Eds. (Springer, 2004), pp. 9–28.
21. Y. Masuyama, Y. Tahara, T. Fukasawa, N. Maeda, Database of sail shapes versus sail performance and validation of numerical calculations for the upwind condition. *J. Mar. Sci. Technol.* **14**, 137–160 (2009).
22. B. Kocivar, Wind car—Land sailer for the highway. *Popular Science* **209**, 102–104 (1976).
23. B. L. Storms *et al.*, "An experimental study of the Ground Transportation System (GTS) model in the NASA Ames 7- by 10-ft wind tunnel" (NASA/TM-2001-209621, NASA Goddard Space Flight Center, 2001).
24. F. N. Beauvais, S. C. Tignor, T. R. Turner, "Problems of ground simulation in automotive aerodynamics" (Pap. 680121, SAE International, 1968).
25. W. H. Hucho, L. J. Janssen, G. Schwarz, "The wind tunnel's ground plane boundary layer–its interference with the flow underneath cars" (Pap. 750066, SAE International, 1975).
26. B. R. McAuliffe, "Improving the aerodynamic efficiency of heavy duty vehicles: Wind tunnel test results of trailer-based drag-reduction technologies" (LTR-AL-2015-0272, National Research Council Canada, 2015).
27. H. Schlichting, *Boundary Layer Theory* (McGraw-Hill, 1960).
28. F. R. Menter, Two-equation eddy-viscosity turbulence models for engineering applications. *AIAA J.* **32**, 1598–1605 (1994).
29. P. J. Roache, Quantification of uncertainty in computational fluid dynamics. *Annu. Rev. Fluid Mech.* **29**, 123–160 (1997).